Effects of Photonic Curing Processing Conditions on $MAPbI_3$ Film Properties and Solar Cell Performance

*Weijie Xu, Trey B. Daunis, Robert T. Piper, and Julia W.P. Hsu**

Department of Materials Science & Engineering, University of Texas at Dallas, Richardson, Texas 75080, United States

KEYWORDS: Photonic curing, perovskite solar cells, high-throughput process, scalable process, methylammonium lead iodide

ABSTRACT. Thermal annealing is the most used post-deposition materials processing method in laboratory research, but due to its slow speed and high energy cost, it is not compatible with the up-scaling and commercialization of perovskite solar cell (PSC) manufacturing. Here, we adapt photonic curing (PC), which uses millisecond light pulses to deliver energy to the sample, to replace thermal annealing for crystallization of methylammonium lead iodide ($MAPbI_3$) films and rapid fabrication of PSCs. We study how PC conditions affect the outcome of $MAPbI_3$ conversion from the precursor to the crystalline perovskite phase by evaluating the films' optical, crystalline, and morphological properties, as well as PSC performance. The results are understood using simulated film temperature profiles. We show that $MAPbI_3$ is readily converted under a wide range of PC conditions. While previous reports all used short pulses (< 3 ms), we find that longer pulses produce more dense films and higher performing PSCs. We achieve a champion power conversion efficiency in a PC processed $MAPbI_3$ PSC of 11.26% under forward scan and 10.34% under reverse scan, with the processing time for the $MAPbI_3$ layer reduced by 30,000-fold, from 10 minutes to 20 milliseconds. Using a 6-inch lamp, spatial uniformity tests show a cross-web efficiency variation of 5%. Our results indicate that using longer pulse lengths, > 10 ms, is the best PC strategy for perovskite conversion, and PC is a promising annealing method for large-area, high-throughput PSC manufacturing.

I. Introduction

Perovskite solar cells (PSCs) have leap-frogged many photovoltaic systems in terms of power conversion efficiency (PCE) in the past decade with their excellent optoelectronic properties and inexpensive solution-processability.[1,2] Increasing manufacturing throughput is the key to realizing PSCs as a major component of the renewable energy portfolio.[3] For example, in a roll-to-roll (R2R) process, a web speed of 30 m/min would enable the production of PSC panels at 3 GW/year capacity.[4] Currently almost all PSCs with high PCE require thermal annealing (TA) to convert precursors to the crystalline perovskite phase. Hotplates are ideal for laboratory scale PSC fabrication due to their simplicity, but ovens are typically used in large-scale manufacturing. At 30 m/min web speed, a typical annealing time of 10-60 minutes[5-7] would require an oven longer than 300 m. In addition, TA is an equilibrium heating method that heats substrates and perovskite films at the same time, which not only incurs a tremendous amount of energy consumption but also causes mechanical failure in flexible plastic devices due to the coefficient of thermal expansion mismatch between different layers.[8-10] Thus, it is necessary to eliminate TA in PSC production.

Recently, photo-irradiation methods including near-infrared radiation,[11] flash infrared-annealing,[12] laser annealing,[13,14] and ultraviolet light[15] have been investigated to replace TA in PSC fabrication because of their fast processing speed and low energy consumption. These studies successfully reduce the processing time of the perovskite active layer from tens of minutes for TA to 2-20 seconds. However, to further reduce capital cost and increase processing speed, a much faster conversion method is needed. A few research groups have reported the use of intense pulsed light or photonic curing (PC) to anneal perovskite films.[16-19] To the best of our

knowledge, it is the only method that can convert perovskite films in less than 1 s. In addition to using PC to process the perovskite active layer, PC has also been used to anneal metal oxide transport layers, e.g. SnO_2[20,21] and TiO_2,[22,23] making an all-PC PSC possible.

PC delivers short (20 μs-100 ms) but intense light pulses from a broadband (200-1500 nm) xenon flash lamp. Perovskite precursor films readily absorb the xenon emission, resulting in crystallization. The absorbance difference between the perovskite precursor film and the transparent substrate causes the perovskite to be selectively heated, hence enabling processing of perovskite films without heating the substrates. While previous work demonstrated the feasibility,[16-19] the effects of processing parameters on perovskite conversion have not been carefully investigated. In this work, we vary PC parameters to study perovskite conversion outcomes which are compared to TA films, with the device structure and processing of all other layers kept constant. The resulting methylammonium lead iodide ($MAPbI_3$) film properties and PSC performance are understood in terms of energy delivered to the sample, light pulse length, and film temperature profiles. We also study the effect of UV light and the uniformity of PC for a realistic manufacturing cross-web dimension, which has not been addressed in previous publications. To explore the practicality of PC in high-throughput manufacturing, all PC experiments were performed under ambient environment.

II. Experimental Section

Materials. PbI_2 was purchased from TCI America, methyl iodide was purchased from GreatCell Solar. All other chemicals were purchased from Sigma-Aldrich. All chemicals were used as purchased.

Perovskite solar cell fabrication. Patterned indium tin oxide (ITO) (Kinetic, 15 ohm/sq) coated glass substrates were cleaned in soapy water, acetone, isopropyl alcohol, and deionized water,

sequentially, and UV-ozone treated for 20 min. Then, NiO hole transport layers were fabricated following Ref. 24. 0.1 M nickel nitrate and acetylacetone were dissolved in 2-methoxyethanol. The solution was kept stirring overnight and filtered through a 0.2 μm polytetrafluoroethylene (PTFE) filter just before spin-coating onto the substrates at 3000 rpm for 30 seconds. The precursor films were dried at 80 °C for 3 min followed by calcination at 250 °C for 45 min. The samples were transferred into a N_2-purged glovebox equipped with a Laurell WS-400BZ-6NPP spin coater as soon as the substrates cooled down to room temperature. $MAPbI_3$ films were deposited and processed following Ref. 5. 50 μL of the precursor solution (equal molar concentration of MAI:PbI_2) was spin-coated at 4000 rpm for 25 s. 1 mL diethyl ether was applied onto the film 11 s after the start of spinning. For TA samples, the $MAPbI_3$ films were annealed at 100 °C for 10 min in the same glovebox. For PC samples, the films were taken to the PulseForge® Invent (500 V/3 A power supply, one capacitor bank, capable of delivering 20 J/cm^2 maximum radiant energy, 150-mm length by 20 mm diameter lamp with 150 mm × 75 mm illumination area) immediately after spin-coating. All PC was performed in air under ambient temperature (22-24 °C) and relative humidity (26-49% RH). The electron transport layer was deposited by spin-coating 13 mg/mL phenyl-C61-butyric acid methylester ($PC_{61}BM$, Solenne BV) in chlorobenzene onto the processed $MAPbI_3$ films at 1200 rpm for 60 s, followed by spin-coating 0.5 mg/mL bathocuproine (BCP, Sigma-Aldrich) in ethanol at 4000 rpm for 30 s. Finally, 100 nm Al was thermally evaporated as the top contact. The diode area is 0.11 cm^2. The device architecture, contact layer materials, and $MAPbI_3$ precursor formulation are optimized for TA samples. All these parameters are the same except for $MAPbI_3$ processing condition between PC and TA samples.

Materials characterization. Unpatterned ITO (Xinyan, 15 ohm/sq) coated glass was used as the substrate for $MAPbI_3$ film characterization by X-ray diffraction (XRD), scanning electron

microscope (SEM), and atomic force microscope (AFM). Glass/ITO/NiO/$MAPbI_3$ layers were prepared as described above. XRD was performed at 3°/min scan speed using a Rigaku SmartLab diffractometer with Cu Kα radiation (λ = 1.5418 Å). Top-view and cross-section SEM images were taken using a Zeiss Supra 40 scanning electron microscope at an acceleration voltage of 10 kV. AFM images were taken using an Asylum MFP-3D. Absorption spectra were measured using an Ocean Optics 4000 USB spectrometer on $MAPbI_3$ films deposited on unpatterned ITO coated glass without the NiO transport layer. The current density-voltage (*J-V*) measurements were conducted under an AM 1.5G 100 mW/cm^2 AAA solar simulator (Abet) using a 2635A Keithley high-sensitivity sourcemeter. A 0.049 cm^2 aperture was used during the measurement. The forward scans were conducted from -0.2 V to 1.2 V and the reverse scans were conducted from 1.2 V to -0.2 V. Both scans were performed at a scan speed of 70 mV/s. All devices were stored in a N_2-filled glovebox in dark overnight before the *J-V* measurement.

Simulation. The film temperature as a function of time, i.e. temperature profile, was simulated using SimPulse® software by Novacentrix. The sample stack is modeled as (from bottom up) 1.1 mm soda lime glass, 155 nm ITO, 450 nm $MAPbI_3$. The thickness of the glass and ITO layers is from the manufacturer. The thickness of $MAPbI_3$ is confirmed by cross-section SEM (Figure S1). Thermal and optical properties of the glass and ITO are based on the SimPulse® database. Properties of $MAPbI_3$ are from Ref. 25-27. Details are given in Table S1.

III. Results and Discussion

Figure 1a shows a schematic representation of the photonic curing on $MAPbI_3$ films. It has been documented that crystallization spontaneously begins in $MAPbI_3$ precursor films when they are exposed to air, resulting in an increase in optical absorbance with time.[18] The optical absorbance of precursor films is critical in the PC process because light absorption determines film temperature

profiles. Thus, every sample was photonically cured within 20 s after spin-coating. During PC, two magnetic strips were used to hold the sample in place on the instrument platform, producing three regions on the sample: material on the two edges is not exposed to light and remains unconverted while the central part is exposed to light. As shown in the picture in Figure 1a, the color of the exposed region is much darker than that of the unexposed regions, evidence that PC, rather than spontaneous crystallization, converts the $MAPbI_3$ precursor film.

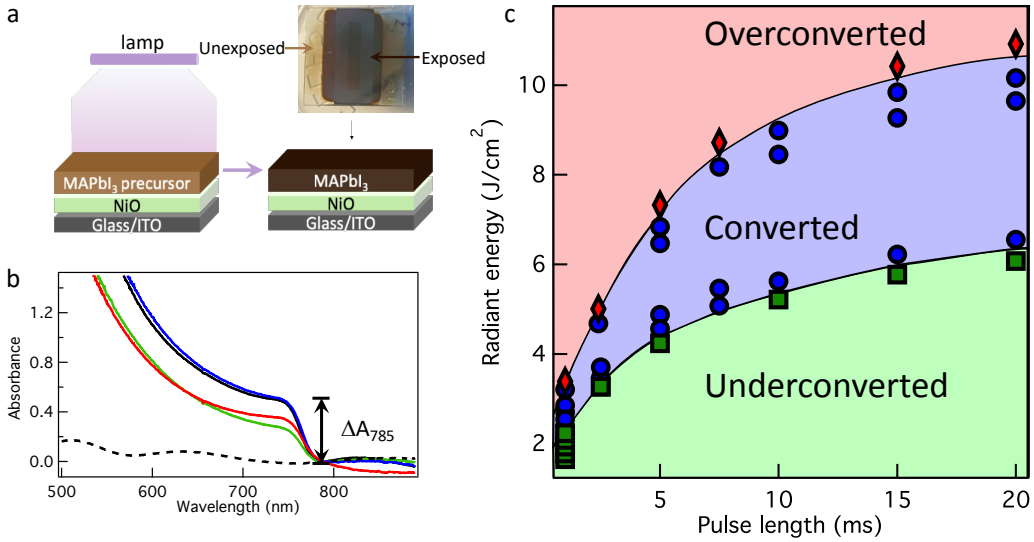

Figure 1. (a) Schematic of the PC process and a photograph of a PC processed $MAPbI_3$ film on a patterned ITO substrate. The center exposed portion is converted $MAPbI_3$ perovskite while the unexposed portions on the sides are precursor. (b) Absorbance of precursor (dashed black line), TA (solid black line), underconverted PC (green line), converted PC (blue line), and overconverted PC (red line) $MAPbI_3$ films. The change in absorbance at 785 nm (ΔA_{785}) is used to classify the outcome of conversion shown in (c) using TA film as the reference, with $\Delta A_{785} < 90\%$ of reference defined as underconverted PC $MAPbI_3$, $\Delta A_{785} > 90\%$ as converted PC $MAPbI_3$, and $\Delta A_{785} < 90\%$ with lower absorbance at shorter wavelengths as overconverted PC $MAPbI_3$. (c) Photonic curing outcome as a function of radiant energy and pulse length classified using the definitions in (b).

Because PC is a high-throughput processing method and can quickly generate many samples, a characterization technique that can match the PC time scale is required to harness the results. We chose UV-vis absorption measurements to evaluate the $MAPbI_3$ film conversion under different PC parameters and to identify representative PC conditions for further detailed characterization. Figure 1b shows absorption spectra for five films that have undergone different processes. The black dashed curve shows the pre-processed $MAPbI_3$ precursor film, which has low absorbance and no distinct onset indicating a band gap. The TA film (black solid curve) shows a clear absorption step at 785 nm. For PC converted films, we applied different pulse conditions and compared the step height at 785 nm (ΔA_{785}) of their absorption spectra to that of the TA reference sample made in the same batch. There are many processing variables in PC, including lamp voltage, pulse length, number of pulses and pulse rate. Lamp voltage determines the overall xenon lamp intensity while pulse length is the time when the lamp is on. It has been shown that halide perovskites can be converted in a single pulse.[16-18] Thus, the independent variables are only lamp voltage and pulse length. While lamp voltage can be controlled directly, the effect on the xenon lamp intensity depends not only on the voltage, but also on lamp size and type, number of capacitor banks, and system configuration. Therefore, a more physically meaningful quantity is the energy per unit area (J/cm^2) delivered to a sample by a single light pulse, i.e. radiant energy, which can be measured using a bolometer. Figure S2 shows the dependence of radiant energy on lamp voltage for different pulse lengths measured for the PulseForge® tool used in this study. A higher lamp voltage produces more radiant energy at a fixed pulse length, and a longer pulse length produces more radiant energy at a fixed lamp voltage. When the radiant energy delivered to the film is low, ΔA_{785} of the PC film is < 90% of the TA reference, which we classify as "underconverted" (Figure 1b green curve). With increasing energy delivered to the film, ΔA_{785} approaches or exceeds

that of the TA film. These PC conditions produce "converted" $MAPbI_3$ films (Figure 1b blue curve). Although ΔA_{785} is a continuous function of energy delivered, we define PC samples with $\Delta A_{785} > 90\%$ of the TA sample as "converted". However, above a certain threshold, excess radiant energy induces degradation in the $MAPbI_3$ films. In these "overconverted" films we observe three distinct differences: a smaller ΔA_{785}, a lower absorbance above the bandgap, and a different curvature in the absorption curve above 800 nm (Figure 1b red curve). Using these criteria, Figure 1c shows the PC outcomes as a function of pulse length (x-axis) and radiant energy (y-axis): green, blue, and red regions represent PC conditions that produce underconverted, converted, and overconverted $MAPbI_3$ films, respectively.

As seen in Figure 1c, at a fixed pulse length, more radiant energy delivered to the sample increases the conversion of $MAPbI_3$ films, while at a fixed radiant energy, longer pulse length results in less converted $MAPbI_3$. To better understand these results, we simulated temperature profiles for $MAPbI_3$ films on glass/ITO for varying radiant energies at fixed pulse lengths of 1 ms and 20 ms (Figure 2a&b), for varying pulse lengths at a fixed radiant energy of 4 J/cm^2 (Figure 2c), and for varying pulse lengths at a fixed lamp voltage of 330 V (Figure 2d). All parameters for simulation are listed in Table S1. At a fixed pulse length, Figure 2a&b show that a higher radiant energy produces a higher peak film temperature (T_p). Additionally, the shape of temperature profiles is different between short (1 ms, Figure 2a) and long (20 ms, Figure 2b) pulse lengths. Under a short pulse length, the film temperature rapidly rises to T_p when the lamp is on (yellow shaded region) and decreases precipitously as soon as the lamp is turned off, resulting in a temperature profile with a steep rise and fall in temperature. Under a long pulse length, the film temperature initially rises quickly as the lamp is turned on, then decreases gradually while the light is on, and shows a change in the slope with a faster decrease rate as the light is turned off. In our

tool, the flash lamp is powered by the electrical energy stored in the capacitor bank, which is drained during long pulses, resulting in decreasing lamp power output. The gradual decrease in film temperature while the lamp is on is due to the film cooling rate exceeding the lamp power output. For the samples in this study and our tool, T_p occurs at ~ 5 ms, at which point the heating rate from the absorption of lamp energy and the cooling rate due to heat loss to the substrate and environment are balanced.

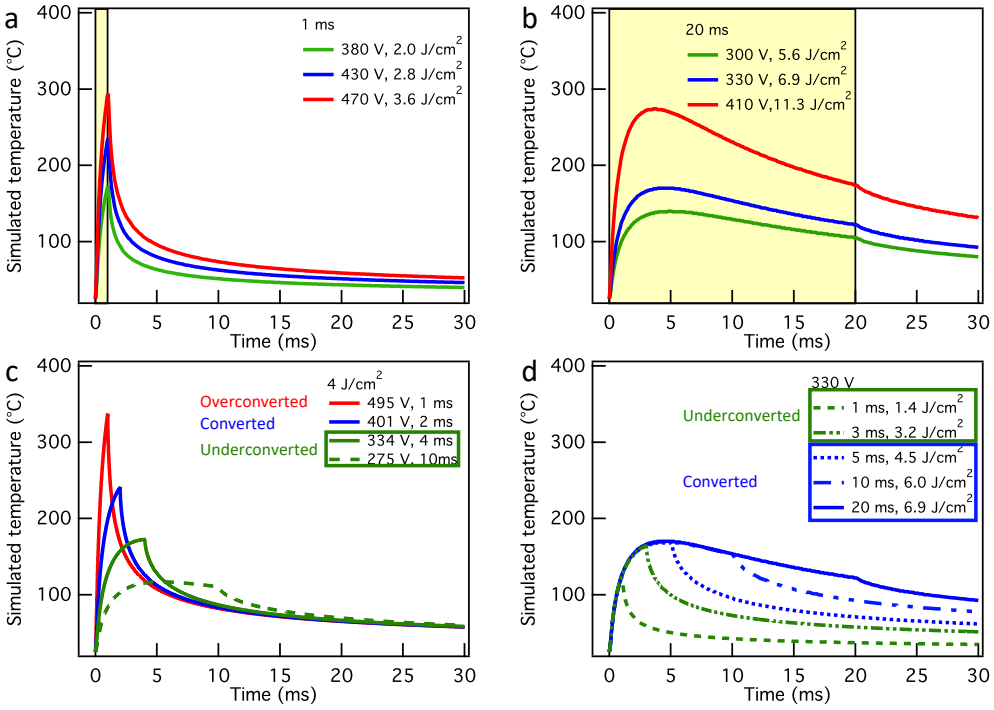

Figure 2. Simpulse® simulations of $MAPbI_3$ film temperature profiles at fixed pulse lengths of (a) 1 ms and (b) 20 ms with different radiant energies. Shaded yellow areas indicate the period when the light is on. (c) Simulated temperature profiles at 4 J/cm² radiant energy with different pulse lengths. (d) Simulated temperature profiles at 330 V lamp voltage with different pulse lengths. The outcome of $MAPbI_3$ films processed using a specific PC condition is shown as green, blue, or red to represent underconverted, converted, or overconverted, respectively.

In contrast, for a fixed radiant energy (Figure 2c), longer pulse lengths allow heat to transfer to the substrate during the pulse, lowering T_p. The large decrease in T_p as pulse length is increased at constant radiant energy is associated with the transition from overconverted, to converted, to underconverted $MAPbI_3$ films when moving from left to right in the processing phase space in Figure 1c. To make this point more clear, the PC outcomes are shown as a function of T_p and pulse length in Figure S3, which shows that conversion requires higher T_p at shorter pulse lengths (< 5 ms). This is because the conversion needs to take place during the short time when the film temperature is elevated (e.g. see Figure 2a) and high temperature is required to achieve a high conversion rate according the Arrhenius law of reaction rate vs. temperature. For longer pulse lengths, the film temperature remains elevated for a longer time as seen in Figure 2b. Thus, even with a lower T_p (and therefore slower rate), there is sufficient time to convert $MAPbI_3$.

From Figure 2d we learn that a sufficient pulse length is needed for the system to reach the maximum temperature (T_{max}) at a given lamp voltage and that T_{max} depends only on lamp voltage. In this example, T_{max} is ~ 170 °C at 330 V. For pulse lengths < 5 ms (Figure 2d two green curves), $T_p < T_{max}$ and depends on the pulse length, with higher T_p for longer pulses. For pulse lengths > 5 ms (Figure 2d three blue curves), $T_p = T_{max}$ and is independent of pulse length. Therefore, for pulses longer than 5 ms, the energy delivered after 5 ms goes to sustain the film temperature, i.e. the tail of the curves in Figure 2b&d, not to increase T_p.

Figure 1c shows that the processing phase space to convert $MAPbI_3$ (blue region) is small, in terms of both pulse length and radiant energy, when the pulse length is shorter than 5 ms. Small variations of PC conditions will greatly impact T_p due to the sharp rise in the temperature profiles; consequently, T_p – and thus extent of conversion – strongly depends on pulse length variation. Our findings help elucidate previously published results. Those studies all used short pulse lengths

(< 3 ms), for which careful control is required to deliver the ideal amount of radiant energy[16] or to optimize the pulse length.[17,18] For pulse lengths > 10 ms, the broader blue region indicates that the perovskite conversion outcomes are less sensitive to variations in PC conditions. In terms of R2R manufacturing, using longer pulse lengths will make the outcome of R2R manufacturing less dependent on variation in web speed, precise synchronization between lamp and sample position, or slight variation in sample thickness.

To study the effects of pulse length and radiant energy on the crystallinity and morphology of perovskite films, we selected 1 ms and 20 ms to represent short and long pulse lengths, respectively, and chose three radiant energy values—low, medium, and high—for each pulse length. The medium radiant energy is the optimal PC processing condition in terms of PSC device performance (discussed below) for the pulse length. PC conditions are summarized in Table 1.

Table 1. Detailed Processing Conditions of $MAPbI_3$ Films to Study Crystallinity, Morphology, and Device Performance (Figure 3-5).

Sample	Annealing method	Lamp voltage (V)	Pulse length (ms)	Peak film temperature (℃)	Radiant energy (J/cm^2)
TA	TA	NA	NA	NA	NA
1ms-Lo	PC	400	1	196	2.4
1ms-Mid	PC	430	1	235	2.9
1ms-Hi	PC	450	1	263	3.3
20ms-Lo	PC	290	20	126	5.2
20ms-Mid	PC	330	20	168	6.9
20ms-Hi	PC	390	20	242	10.2

XRD is performed to confirm that $MAPbI_3$ perovskite crystalline phase can be formed in the millisecond timeframe of PC. Figure 3a shows the XRD patterns for $MAPbI_3$ films processed by different 20-ms-PC conditions and TA. Perovskite is the dominant crystalline phase in all samples,[25] as is evident by strong signals in major reflections—(110) and (220)—that match the $MAPbI_3$ tetragonal (I4cm) crystalline structure. Similar XRD patterns are found for 1-ms-PC $MAPbI_3$ films (Figure S4a). In addition, the two samples processed under high radiant energy conditions (20ms-Hi, 1ms-Hi) show a clear PbI_2 peak ((001) at 12.7°). However, all PC samples have lower PbI_2 XRD signals than the TA film, suggesting that PC prevents PbI_2 from crystallizing out of the $MAPbI_3$ films, consistent with previous reports.[17,18] We speculate that this phenomenon is the result of a kinetic limitation to form a thermodynamically stable PbI_2 phase in such a short time.

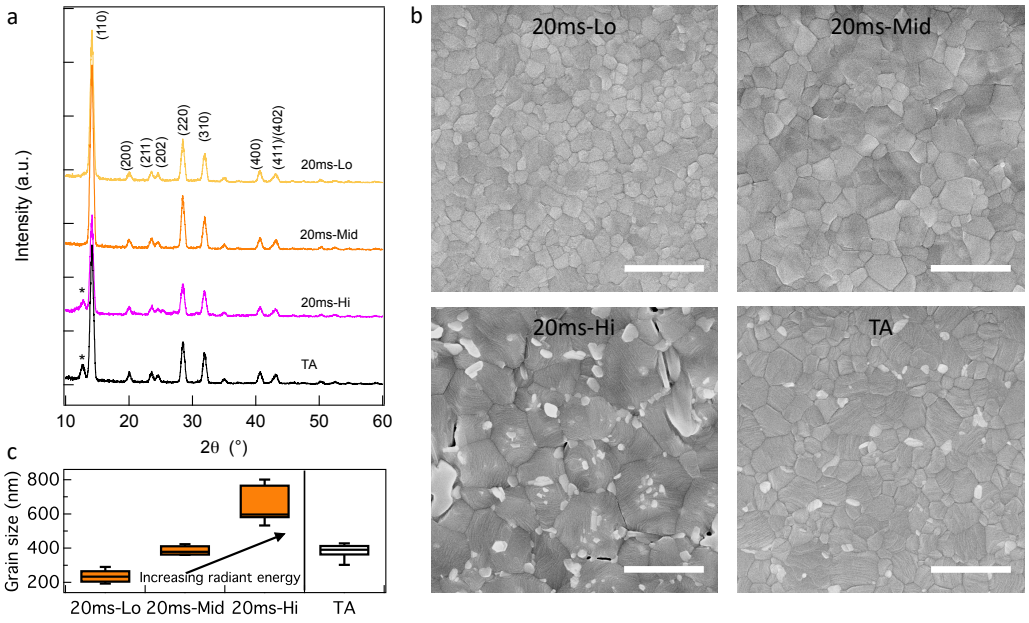

Figure 3. TA and PC processed (20 ms pulse length under different radiant energies) ITO/NiO/$MAPbI_3$ samples: (a) XRD patterns, (b) top-view SEM images (scale bar = 1 μm), and (c) statistical analysis of grain sizes from low-magnification SEM images (Figure S5).

We also performed SEM on these samples to understand the effect of PC conditions on $MAPbI_3$ film morphology. Figure 3b shows top-view SEM images of 20-ms-PC and TA $MAPbI_3$ films. We used ASTM E112-13[28] to statistically analyze the grain size from low-magnification SEM images (Figure S5). Results show that the average grain size of $MAPbI_3$ increases with radiant energy under 20 ms pulse length (Figure 3c). Similar results are found for 1-ms-PC $MAPbI_3$ films (Figure S4b&c). It was reported that higher annealing temperatures produce larger grains due to reduced nucleation rates and higher growth rates.[29] A recent study on laser induced conversion of $MAPbI_3$ also showed that higher laser powers produce larger grain size.[13] Thus, grain size increases, due to a higher growth rate or Oswald ripening, with PC radiant energy as a result of the higher film temperature reached during crystallization. However, when radiant energy exceeds a certain threshold PbI_2 appears. The two high radiant energy samples (1ms-Hi, 20ms-Hi) have visible PbI_2 crystals (light-color areas in Figure 3b&S4b),[30] consistent with XRD results (Figure 3a&S4a). It is known that larger grain size is favorable for PSC performance due to mitigation of trap states or carrier blocking at grain boundaries.[2] 1ms-Mid and 20ms-Mid are optimized to have the largest grain size without PbI_2 phase for each pulse length. Typical material properties are summarized in Table 2.

In high-magnification SEM images of these samples (Figure S6), we observe obvious step-bunching within the grains in all samples, but particularly in 1ms-Hi, 20ms-Hi, and TA samples. For a fixed pulse length, samples processed with higher radiant energy exhibit more pronounced step-bunching—taller steps and wider terraces between steps—than those processed with lower radiant energy. No detailed study of step-bunching in polycrystalline halide perovskite films has been performed to our knowledge, but similar features have been reported on single-crystal perovskite.[31,32] We suggest that this is caused by misorientation between the grains' fastest growth

Table 2. Summary of Material Properties of $MAPbI_3$ with Different Processing

Sample	XRD peak intensity ratio (12.7°/14.1°)	Average grain size (nm)	Normalized ΔA_{785}[a]
TA	0.15	382	1.00
1ms-Lo	0.05	344	0.95
1ms-Mid	0.05	436	1.20
1ms-Hi	0.10	504	0.90
20ms-Lo	0.06	236	0.71
20ms-Mid	0.04	385	1.00
20ms-Hi	0.15[b]	648	0.93

[a] Normalized to TA sample
[b] The intensity of $MAPbI_3$ (110) reflection at 14.1° is smaller than that of TA. See Figure 3a.

direction and the surface normal. Step-bunching has been reported to depend on annealing/growth temperature in other materials systems, e.g. SiC[33] and graphene,[34] with higher temperatures induce more severe step-bunching. Our results are consistent with higher film temperatures, reached under higher radiant energies, promote step-bunching. The TA sample exhibits more obvious step-bunching compared with the optimized PC sample (20ms-Mid) despite similar grain size. To quantitatively analyze this topography feature, we performed AFM measurements on these samples. Figure 4a shows AFM topography images of 20ms-PC and TA $MAPbI_3$ films. Similar to high-magnification SEM images, we observed a more pronounced step-bunching feature in the 20ms-Hi and TA films. Line cuts on the 20ms-Mid and TA films confirm that the TA film has a step height and width of ~ 4 nm and the 20ms-Mid film has a step height and width of ~ 1 nm (Figure 4b). We suggest that this is caused by the much longer annealing time (10 min) compared to PC samples (20 ms). Longer time at elevated temperature allows for motion and rearrangement of surface atoms, facilitating step-bunching to lower surface free energy.[33] However, this step-

bunching feature does not increase film roughness. It is the grain to grain variation that contributes to the film roughness. For example, the roughness of the TA film is 7.45 ± 0.26 nm whereas the roughness of 20ms-Mid is 10.33 ± 0.40 nm (Figure 4c). Figure 4c also shows that the roughness of the PC $MAPbI_3$ films increases with the radiant energy, which can be attributed to the additional PbI_2 crystals on top of $MAPbI_3$ grains (Figure 3b) and the larger grain size variation (Figure 3c).

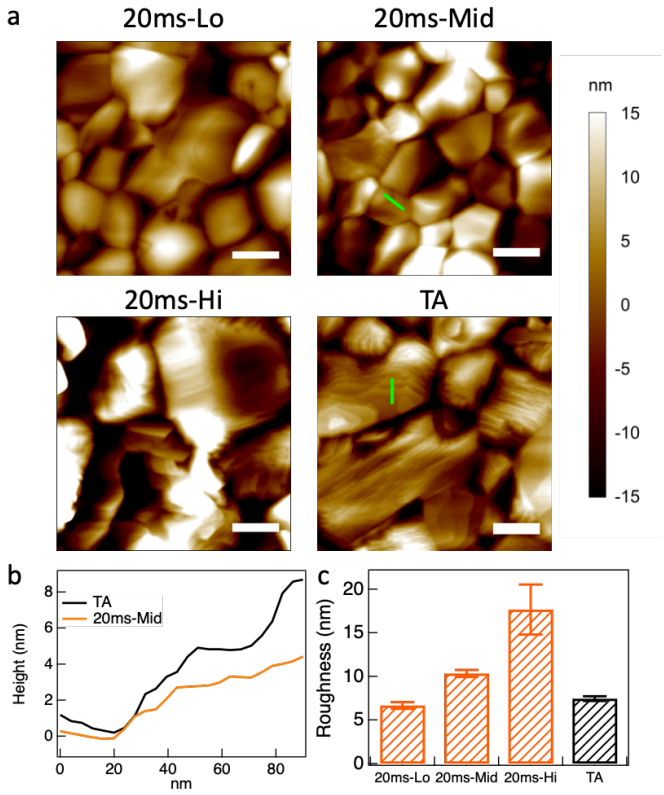

Figure 4. (a) AFM images of TA and 20ms-PC processed $MAPbI_3$ films (scale bar = 200 nm). (b) Line cuts along green lines in (a). (c) Average roughness calculated from 1 μm × 1 μm AFM images taken at three different locations for each sample.

Figure 5a compares *J-V* behaviors under AM 1.5G illumination for representative underconverted (green), converted (blue), and overconverted (red) PC processed $MAPbI_3$ solar cells. The underconverted device has a low short-circuit current density (J_{sc}) and high series

resistance, while the overconverted device is shorted. Only the converted device exhibits good *J-V* characteristics. To understand how PC conditions affect the solar cell device parameters, we fixed the pulse length at 1 ms or 20 ms and varied the radiant energy by increasing lamp voltage at 10 V increments in the underconverted and converted regions (Figure 5b). We do not include the overconverted $MAPbI_3$ films because those devices are shorted. The corresponding radiant energy is recorded. V_{oc} is constant at low and medium radiant energy for films processed using both 1 ms and 20 ms—with the exception of 1ms-Lo—and decreases at high radiant energy. For films processed at 1 (20) ms, V_{oc} begins to decrease above 3.0 (9.5) J/cm^2. When the radiant energy reaches these values, the processing condition is closer to the red region of Figure 1c, the films become rougher (Fig. 4c), and $MAPbI_3$ starts to decompose. Thus, the devices become shunted with lower V_{oc}. The maximum V_{oc} achieved at 20 ms is higher than at 1 ms. J_{sc} behavior is different from V_{oc} and is similar for 1 ms and 20 ms. For both pulse lengths, maximum J_{sc} values are achieved in the intermediate radiant energy range, with a larger range for 20 ms—from 6.9 to 7.9 J/cm^2. Fill factor (FF) for 1 ms pulse length is constant, while for 20 ms it slightly decreases with increasing radiant energy. Below 7.9 J/cm^2, FF for the 20 ms pulse length is higher than that for the 1 ms. Consequently, PCE exhibits a maximum at an intermediate radiant energy, with 20 ms pulse length producing a higher PCE than 1 ms, primarily due to FF and V_{oc}. Comparing the morphology of optimized $MAPbI_3$ films processed at the two pulse lengths (Figure 5c), we notice that the morphology of 1ms-Mid film is porous whereas that of 20ms-Mid film is dense and fully-covered. The different temperature profiles at short and long pulse lengths can explain this morphology difference. As discussed above, a shorter pulse length requires a higher T_p to achieve conversion. The high heating and cooling rates in these processing conditions produce thermal stress in the film that can result in cracks and less dense films, as seen in all 1 ms processed films (Figure S4b

& S5a-c). The porous film morphology is most likely responsible for 1-ms devices' low V_{oc} and FF values, and consequently inferior performance.

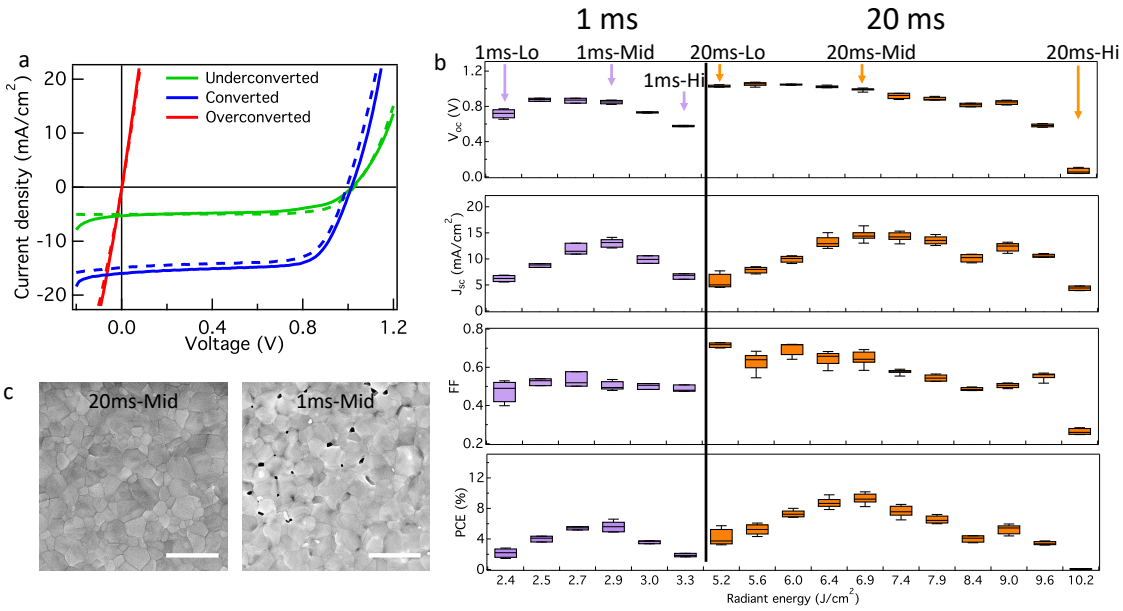

Figure 5. (a) *J-V* curves for representative PSCs with $MAPbI_3$ processed in underconverted (green), converted (blue), and overconverted (red) regions of Figure 1(c). Solid lines are forward scans and dashed lines are reverse scans. (b) Statistical analysis of device parameters (reverse scan) for underconverted and converted $MAPbI_3$ films photonically cured with 1 ms and 20 ms pulses at different radiant energies. (c) Top-view SEM images (scale bar = 1 μm) of ITO/NiO/$MAPbI_3$ stacks processed at optimized radiant energy under 1 ms and 20 ms pulse.

Figure 6a&b show the comparison between the champion PC device (20ms-Mid) with the state-of-the-art TA device. The device parameters are given in Table S2. The V_{oc} for the PC device is comparable to the TA device, indicating a similar band alignment and pin-hole free coverage of $MAPbI_3$ films.[35] The lower FF in the PC device may be attributed to a higher series resistance and a larger roughness of the PC films. The difference in J_{sc} is the primary contributor to the PCE difference between PC and TA devices. We suggest this is due to the processing time difference

between PC and TA. As Figure 4a&b shows, the morphology is different between TA and PC samples, with more pronounced step-bunching—taller steps and wider terraces between steps—in the TA sample than in the 20ms-Mid sample. For graphene, taller steps and wider terraces have been attributed to better electrical properties and charge transport.[34] We speculate that the high J_{sc} observed in TA samples might also result from the taller steps and larger terrace widths. Furthermore, to demonstrate the potential of PC in R2R manufacturing, all our PC devices were fabricated in an ambient environment. The sensitivity of $MAPbI_3$ to moisture may also negatively affect the PC device performance.[36] While overall PC device performance is inferior to TA devices, it is still respectable (11.26% PCE under forward scan and 10.34% PCE under reverse scan). Most importantly, the processing time is 30,000-fold shorter than TA (Figure 6c), a necessary requirement for high-throughput manufacturing.

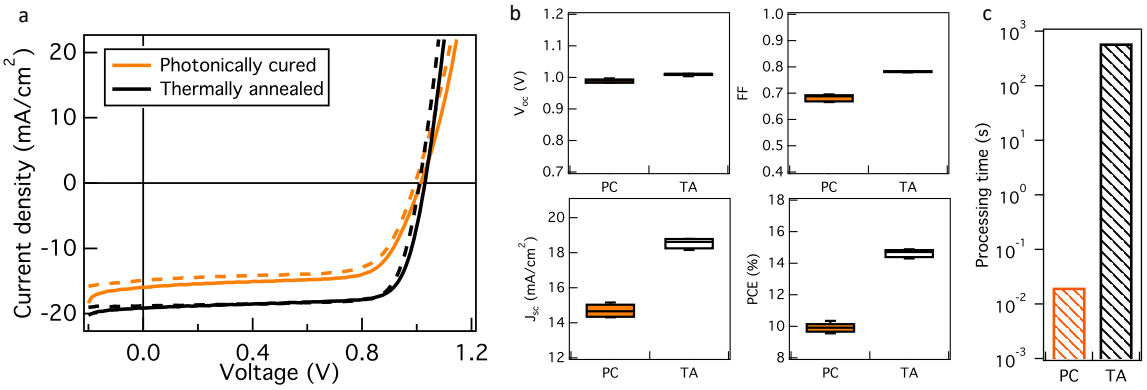

Figure 6. (a) *J-V* curves of PC and TA champion devices. (b) Statistical analysis of device parameters (reverse scan) from the same batch (5 devices each) as (a). (c) Processing time comparison for PC and TA.

One concern of PC on $MAPbI_3$ is the possible degradation due to UV illumination during PC.[18,37] To test this, we inserted a UV-absorbing glass slide between the precursor film and the lamp during PC. It blocks 97% of light with wavelength below 320 nm (Figure S7a). To compensate for the

radiant energy loss caused by adding this UV filter, we increased the lamp voltage. Figure S7b shows that the sample with $MAPbI_3$ covered by the UV-absorbing glass slide during PC does not out-perform the devices made in the same batch without the UV-absorbing glass. Two factors can contribute to this result: (1) the amount of UV light generated by the xenon flash lamp is low,[38] and (2) the time that $MAPbI_3$ is exposed to UV light in PC is much shorter compared to previous studies on UV degradation effects.[39] To the best of our knowledge, the effect of UV light on perovskite films in a millisecond time frame has not been studied.

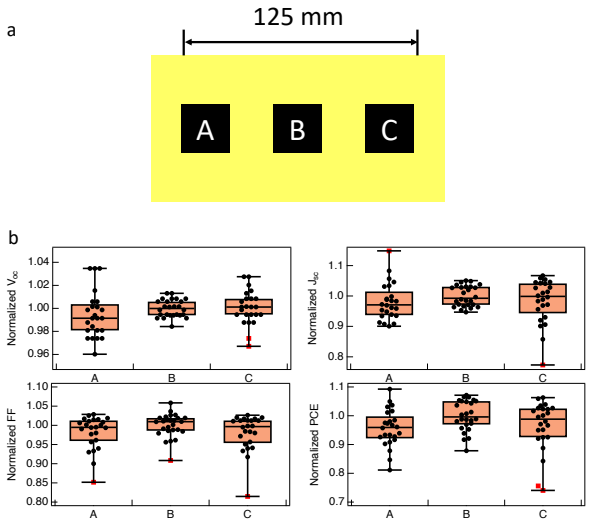

Figure 7. (a) Schematics of the uniformity test. The yellow rectangle represents the area covered by the light pulse (150 mm × 75 mm). Black squares represent the location and the size of samples (25 mm × 25 mm). The PC condition was a 20 ms pulse length at 6.9 J/cm^2. (b) Statistical analysis of device parameters (reverse scan) for samples processed at the 3 different locations (≥ 24 devices each).

Finally, we test the uniformity of PC process on a length scale that is practical for manufacturing. PSCs with $MAPbI_3$ films placed at different locations linearly along the lamp (cross-web) when undergoing PC are evaluated. Figure 7a depicts the schematic representation of our cross-web

uniformity test. Position B is at the center of the area covered by the light in our tool (yellow rectangle) and represents devices fabricated at the center of a roll. It is also the position used to process all $MAPbI_3$ films shown in Figure 1-6. Positions A and C represent devices at the edges of a roll. Figure 7b shows the variation in device parameters of samples processed at locations A, B, and C. Based on at least 24 devices each, the variation of average PCE values vary by ~ 5% from the center to the edges. These results provide insight into the large-area uniformity in a real R2R situation.

IV. Conclusion

We study the effects of PC parameters on $MAPbI_3$ film properties and solar cell performance. The PC processing outcomes on $MAPbI_3$ are classified using UV-vis absorption spectra. The range of radiant energy and pulse lengths for successful $MAPbI_3$ conversion is broader at long pulse lengths (> 10 ms), attributed to more gentle temperature profiles and the independence of T_p on pulse length. Thus, these operation conditions are less susceptible to small process variation in R2R manufacturing. $MAPbI_3$ films processed using a long pulse length also show a more dense morphology with superior device performance. For a fixed pulse length, we found that the grain size increases with radiant energy and the solar cell performance is optimized at intermediate energy (middle of the converted region) due to maximized J_{sc}. We achieve a PC champion device with a PCE of 11.26% (forward scan); while it is not as high as our state-of-the-art TA reference of 15.03% (forward scan), the processing time is reduced by 30,000-fold. We note that with careful optimization on perovskite precursor formulation, Ankireddy et al. reported a PCE of 15.3% in a PSC processed by PC.[19] Thus, the understanding gained from our current study, combined with previous demonstrations, presents a strong support for PC as a viable technology for high-throughput PSC manufacturing.

In our research tool, the maximum repetition rate for the optimal PC conditions shown here is 0.3 Hz. With the current configuration, the down-web processing length is 75 mm and the web speed is 1.35 m/min with 5% cross-web PCE variation. With an industrial PC tool, e.g. one with a 500V/45 A power supply—allowing for a faster repetition rate with the same pulse conditions—and 150 mm down-web processing length per pulse, the web speed can be straightforwardly upscaled to 40 m/min. In a continuous R2R process, overlapping pulses may be necessary to achieve uniform film properties along the length of the web. While this will lower the web speed, a high web speed can still be maintained. With up to four overlapping pulses, for example, the above processing condition will result in a minimum web speed of 10 m/min, with higher speeds possible due to the reduced energy required for each pulse. Moreover, additional lamps can be used to increase overlapping exposure areas while maintaining web speed. Therefore, photonic curing is well suited to replace thermal annealing in high-throughput PSC manufacturing.

ASSOCIATED CONTENT

Supporting Information. Cross-section SEM images of $MAPbI_3$ films; The relationship of radiant energy with lamp voltage; Process phase map as function of peak film temperature and pulse length; XRD results on 1ms-PC $MAPbI_3$ films. Low/high-magnification SEM images of $MAPbI_3$ films; Comparison of device performance with/without UV filter; Simulation parameters used in temperature profile; Champion device parameters.

AUTHOR INFORMATION

Corresponding Author

* jwhsu@utdallas.edu

Author Contributions

J.W.P.H. and T.B.D. conceived the idea. W.X. designed the experiment and performed all experimental work. R.T.P. participated in NiO deposition and devices fabrication. W.X. wrote the 1st draft of the manuscript. All authors discussed the data and edited the manuscript. All author have given approval to the final version of the manuscript.

Notes

The authors declare no competing financial interest.

ACKNOWLEDGMENT

This material is based upon work supported by the U.S. Department of Energy's Office of Energy Efficiency and Renewable Energy (EERE) under the Solar Energy Technology Office Award Number DE-EE0008544. J.W.P.H. acknowledges support from the Texas Instruments Distinguished Chair in Nanoelectronics. We thank M. Quevedo for the use of their glovebox, K. Schroder for photonic curing discussion, and W. Dunlop-Shohl for answering perovskite solar cells fabrication questions.

Disclaimer

or otherwise does not necessarily constitute or imply its endorsement, recommendation, or favoring by the United States Government or any agency thereof. The views and opinions of authors expressed herein do not necessarily state or reflect those of the United States Government or any agency thereof.

REFERENCES

(1) Jena, A. K.; Kulkarni, A.; Miyasaka, T. Halide Perovskite Photovoltaics: Background, Status, and Future Prospects. Chem. Rev. 2019, 119 (5), 3036–3103.

(2) Dunlap-Shohl, W. A.; Zhou, Y.; Padture, N. P.; Mitzi, D. B. Synthetic Approaches for Halide Perovskite Thin Films. Chem. Rev. 2018, 119 (5), 3193–3295.

(3) Song, Z.; McElvany, C. L.; Phillips, A. B.; Celik, I.; Krantz, P. W.; Watthage, S. C.; Liyanage, G. K.; Apul, D.; Heben, M. J. A Technoeconomic Analysis of Perovskite Solar Module Manufacturing with Low-Cost Materials and Techniques. Energy Environ. Sci. 2017, 10, 1297–1305.

(4) http://www.enmatcorp.com

(5) Ahn, N.; Son, D.-Y.; Jang, I.-H.; Kang, S. M.; Choi, M.; Park, N.-G. Highly Reproducible Perovskite Solar Cells with Average Efficiency of 18.3% and Best Efficiency of 19.7% Fabricated via Lewis Base Adduct of Lead(II) Iodide. J. Am. Chem. Soc. 2015, 137 (27), 8696–8699.

(6) Correa-Baena, J.-P.; Steier, L.; Tress, W.; Saliba, M.; Neutzner, S.; Matsui, T.; Giordano, F.; Jacobsson, T. J.; Srimath Kandada, A. R.; Zakeeruddin, S. M.; Petrozza, A.; Abate, A.; Nazeeruddin, M. K.; Grätzel, M.; Hagfeldt, A. Highly Efficient Planar Perovskite Solar Cells Through Band Alignment Engineering. Energy Environ. Sci. 2015, 8 (10), 2928–2934.

(7) Saliba, M.; Correa-Baena, J.-P.; Wolff, C. M.; Stolterfoht, M.; Phung, N.; Albrecht, S.; Neher, D.; Abate, A. How to Make Over 20% Efficient Perovskite Solar Cells in Regular (N–I–P) and Inverted (P–I–N) Architectures. Chem Mater 2018, 30 (13), 4193–4201.

(8) Bush, K. A.; Rolston, N.; Gold-Parker, A.; Manzoor, S.; Hausele, J.; Yu, Z. J.; Raiford, J. A.; Cheacharoen, R.; Holman, Z. C.; Toney, M. F.; Dauskardt, R. H.; McGehee, M. D. Controlling Thin-Film Stress and Wrinkling During Perovskite Film Formation. ACS Energy Letters 2018, 3 (6), 1225–1232.

(9) Cheacharoen, R.; Rolston, N.; Harwood, D.; Bush, K. A.; Dauskardt, R. H.; McGehee, M. D. Design and Understanding of Encapsulated Perovskite Solar Cells to Withstand Temperature Cycling. Energy Environ. Sci. 2017, 1–7.

(10) Daunis, T. B.; Schroder, K. A.; Hsu, J. W. P. Photonic Curing of Solution-Deposited ZrO2 Dielectric on PEN: a Path Towards High-Throughput Processing of Oxide Electronics. npj Flexible Electronics 2020, 1–7.

(11) Troughton, J.; Charbonneau, C.; Carnie, M. J.; Davies, M. L.; Worsley, D. A.; Watson, T. M. Rapid Processing of Perovskite Solar Cells in Under 2.5 Seconds. Journal of Materials Chemistry A 2015, 3 (17), 9123–9127.

(12) Sanchez, S.; Hua, X.; Phung, N.; Steiner, U.; Abate, A. Flash Infrared Annealing for Antisolvent-Free Highly Efficient Perovskite Solar Cells. Adv. Energy Mater. 2018, 8 (12), 1702915.

(13) Konidakis, I.; Maksudov, T.; Serpetzoglou, E.; Kakavelakis, G.; Kymakis, E.; Stratakis, E. Improved Charge Carrier Dynamics of $CH_3NH_3PbI_3$ Perovskite Films Synthesized by Means of Laser-Assisted Crystallization. ACS Applied Energy Materials 2018, 1 (9), 5101–5111.

(14) You, P.; Li, G.; Tang, G.; Cao, J.; Yan, F. Ultrafast Laser-Annealing of Perovskite Films for Efficient Perovskite Solar Cells. Energy Environ. Sci. 2020, 13 (4), 1187–1196.

(15) Ouyang, Z.; Abrams, H.; Bergstone, R.; Li, Q.; Zhu, F.; Li, D. Rapid Layer-Specific Annealing Enabled by Ultraviolet LED with Estimation of Crystallization Energy for High-Performance Perovskite Solar Cells. Adv. Energy Mater. 2019, 10 (4), 1902898–10.

(16) Lavery, B. W.; Kumari, S.; Konermann, H.; Draper, G. L.; Spurgeon, J.; Druffel, T. Intense Pulsed Light Sintering of $CH_3NH_3PbI_3$ Solar Cells. ACS Appl. Mater. Interfaces 2016, 8 (13), 8419–8426.

(17) Troughton, J.; Carnie, M. J.; Davies, M. L.; Charbonneau, C.; Jewell, E. H.; Worsley, D. A.; Watson, T. M. Photonic Flash-Annealing of Lead Halide Perovskite Solar Cells in 1 ms. Journal of Materials Chemistry A 2016, 4 (9), 3471–3476.

(18) Muydinov, R.; Seeger, S.; Kumar, S. H. B. V.; Klimm, C.; Kraehnert, R.; Wagner, M. R.; Szyszka, B. Crystallisation Behaviour of $CH_3NH_3PbI_3$ Films_ the Benefits of Sub-Second Flash Lamp Annealing. Thin Solid Films 2018, 653, 204–214.

(19) Ankireddy, K.; Ghahremani, A. H.; Martin, B.; Gupta, G.; Druffel, T. Rapid Thermal Annealing of $CH_3NH_3PbI_3$ perovskite Thin Films by Intense Pulsed Light with Aid of Diiodomethane Additive. Journal of Materials Chemistry A 2018, 6 (20), 9378–9383.

(20) Ghahremani, A. H.; Martin, B.; Gupta, A.; Bahadur, J.; Ankireddy, K.; Druffel, T. Rapid Fabrication of Perovskite Solar Cells Through Intense Pulse Light Annealing of SnO_2 and Triple Cation Perovskite Thin Films. Materials & Design 2020, 185 (C), 108237.

(21) Zhu, M.; Liu, W.; Ke, W.; Clark, S.; Secor, E. B.; Song, T.-B.; Kanatzidis, M. G.; Li, X.; Hersam, M. C. Millisecond-Pulsed Photonically-Annealed Tin Oxide Electron Transport Layers for Efficient Perovskite Solar Cells. Journal of Materials Chemistry A 2017, 5 (46), 24110–24115.

(22) Das, S.; Gu, G.; Joshi, P. C.; Yang, B.; Aytug, T.; Rouleau, C. M.; Geohegan, D. B.; Xiao, K. Low Thermal Budget, Photonic-Cured Compact TiO_2 layers for High-Efficiency Perovskite Solar Cells. Journal of Materials Chemistry A 2016, 4 (24), 9685–9690.

(23) Feleki, B.; Bex, G.; Andriessen, R.; Galagan, Y.; Di Giacomo, F. Rapid and Low Temperature Processing of Mesoporous TiO_2 for Perovskite Solar Cells on Flexible and Rigid Substrates. Materials Today Communications 2017, 13, 232–240.

(24) Liu, Z.; Chang, J.; Lin, Z.; Zhou, L.; Yang, Z.; Chen, D.; Zhang, C.; Liu, S. F.; Hao, Y. High-Performance Planar Perovskite Solar Cells Using Low Temperature, Solution-Combustion-Based Nickel Oxide Hole Transporting Layer with Efficiency Exceeding 20%. Adv. Energy Mater. 2018, 8 (19), 1703432–1703439.

(25) Stoumpos, C. C.; Malliakas, C. D.; Kanatzidis, M. G. Semiconducting Tin and Lead Iodide Perovskites with Organic Cations: Phase Transitions, High Mobilities, and Near-Infrared Photoluminescent Properties. Inorganic Chemistry 2013, 52 (15), 9019–9038.

(26) Heiderhoff, R.; Haeger, T.; Pourdavoud, N.; Hu, T.; Al-Khafaji, M.; Mayer, A.; Chen, Y.; Scheer, H.-C.; Riedl, T. Thermal Conductivity of Methylammonium Lead Halide Perovskite Single Crystals and Thin Films: a Comparative Study. J. Phys. Chem. C 2017, 121 (51), 28306–28311.

(27) Onoda-Yamamuro, N.; Matsuo, T.; Suga, H. Calorimetric and IR Spectroscopic Studies of Phase Transitions in Methylammonium Trihalogenoplumbates (II)†. Journal of Physics and Chemistry of Solids 1990, 51 (12), 1383–1395.

(28) Standard, A. Standard Test Methods for Determining Average Grain Size. ASTM Int E 2012, 112–112.

(29) Zhou, Y.; Game, O. S.; Pang, S.; Padture, N. P. Microstructures of Organometal Trihalide Perovskites for Solar Cells: Their Evolution From Solutions and Characterization. J. Phys. Chem. Lett. 2015, 6 (23), 4827–4839.

(30) Pool, V. L.; Dou, B.; Van Campen, D. G.; Klein-Stockert, T. R.; Barnes, F. S.; Shaheen, S. E.; Ahmad, M. I.; van Hest, M. F. A. M.; Toney, M. F. Thermal Engineering of $FAPbI_3$ Perovskite Material via Radiative Thermal Annealing and in Situ XRD. Nature Communications 2017, 8 (1), 1–8.

(31) Ding, J.; Zhao, Y.; Sun, Y.; Du, S.; Cui, H.; Jing, L.; Cheng, X.; Zuo, Z.; Zhan, X. Atomic Force Microscopy Investigation of a Step Generation and Bunching on the (100) Facet of a $CH_3NH_3PbI_3$ crystal, Grown From Γ-Butyrolactone. Crystal Research and Technology 2017, 52 (4), 1700021–1700025.

(32) Li, H.-D.; Xu, Z.-W.; Fu, Q.-M.; Zhao, H.-Y.; Ding, J.-X.; Ma, Y.-F.; Han, Y.-B.; He, R.; Shi, L.; Wang, S.-G.; Ma, Z.-B. The Role of Mn as Dopant on the Optoelectronic Properties of $MA(Pb_{1-x}Mn_x)Cl_3$ single Crystals. Mater. Res. Express 2019, 6 (8), 086210–086218.

(33) Syväjärvi, M.; Yakimova, R.; Janzén, E. Step-Bunching in SiC Epitaxy: Anisotropy and Influence of Growth Temperature. Journal of Crystal Growth 2002, 236 (1-3), 297–304.

(34) Bao, J.; Yasui, O.; Norimatsu, W.; Matsuda, K.; Kusunoki, M. Sequential Control of Step-Bunching During Graphene Growth on SiC (0001). Appl. Phys. Lett. 2016, 109 (8), 081602–081606.

(35) Carnie, M. J.; Charbonneau, C.; Davies, M. L.; Regan, B. O.; Worsley, D. A.; Watson, T. M. Performance Enhancement of Solution Processed Perovskite Solar Cells Incorporating Functionalized Silica Nanoparticles. Journal of Materials Chemistry A 2014, 2 (40), 17077–17084.

(36) Wang, R.; Mujahid, M.; Duan, Y.; Wang, Z.-K.; Xue, J.; Yang, Y. A Review of Perovskites Solar Cell Stability. Adv. Funct. Mater. 2019, 29 (47), 1808843–25.

(37) Ghahremani, A. H.; Martin, B.; Ankireddy, K.; Druffel, T. Rapid Processing of Perovskite Solar Cells Through Pulsed Photonic Annealing: a Review. Journal of Coatings Technology and Research 2019, 16 (6), 1637–1642.

(38) https://www.novacentrix.com/FAQ

(39) Lee, S.-W.; Kim, S.; Bae, S.; Cho, K.; Chung, T.; Mundt, L. E.; Lee, S.; Park, S.; Park, H.; Schubert, M. C.; Glunz, S. W.; Ko, Y.; Jun, Y.; Kang, Y.; Lee, H.-S.; Kim, D. UV Degradation and Recovery of Perovskite Solar Cells. Scientific Reports 2016, 6 (1), 6050–10.